RSC Advances

PAPER

View Article Online
View Journal | View Issue

Cite this: *RSC Adv.*, 2025, **15**, 1766

Optimizing the properties of In–N dual-doped SnO_2 films: incorporation of nitrogen into the SnO_2 lattice at the optimal content *via* direct current sputtering

Tran Le *[ab]

Received 1st December 2024
Accepted 14th January 2025

DOI: 10.1039/d4ra08468c

rsc.li/rsc-advances

Direct current magnetron sputtering was employed to fabricate In–N dual-doped SnO_2 films, with varying concentrations of N_2 in a mixed sputtering gas of N_2 and argon (Ar). The quantity of *N*-substituted O elements in the SnO_2 lattice was confirmed through energy-dispersive X-ray spectroscopy (EDX) and X-ray photoelectron spectroscopy (XPS). A comprehensive investigation of properties of the In–N dual-doped SnO_2 films was conducted using various techniques, including X-ray diffraction analysis, field-emission scanning electron microscopy (FESEM), atomic force microscopy (AFM), ultraviolet absorption spectroscopy, Hall effect measurements, and current–voltage (*I*–*V*) characteristic assessments. The results indicated that when the ratio of N_2 to the mixed gas (Ar + N_2) exceeded 15%, the films exhibited p-type conductivity. The films demonstrated optimal electrical and structural properties at an N_2 content of 45%, with a resistivity of 5.1×10^{-3} Ω cm, hole mobility of 12.75 $cm^2\ V^{-1}\ s^{-1}$, crystal grain size of 25.74 nm, and a root mean square (RMS) roughness of 0.61 nm, resulting in the highest photocurrent at the INTO-45/Si interface.

1. Introduction

Semiconductor technology has consistently advanced to fulfill societal demands. Semiconductor chip technology has achieved unparalleled levels of downsizing. As the semiconductor industry progresses, continuous research on transparent conductive oxides (TCOs) continues in pursuit of additional advancements. TCOs, which include n- and p-type semiconductors, are utilized in opto-electronic devices such as solar cells,[1–10] various LED types,[11–16] transparent transistors,[17–19] thermochromic windows,[20–22] and electrochromic windows.[23–25] Although n-type TCOs have demonstrated encouraging outcomes, ongoing research focuses on p-type TCOs to broaden their utilization in opto-electronic systems. As detailed in the literature, n-type TCOs as In_2O_3 doped with Sn (ITO), ZnO doped with group III metal elements, and SnO_2 doped with F, Sb, or Ta not only have great optical transparency but also possess remarkable conductivity. This is due to the fact that nearly all defects in the host lattice act as donors without being accompanied by a charge compensation effect, along with the presence of native oxygen vacancies (V_O). Conversely, p-type transparent conductive oxides (TCOs) such as ZnO or SnO_2 have not been able to reach the requisite level of electrical conductivity. This is because there is a charge compensation interaction between substituted acceptors and native donors such as V_O or interstitial dopants. The introduction of group I metals, including Na,[26,27] Ag,[28] and Li,[29] or group V elements such as N,[30] P,[31] and As[32] into ZnO results in a low density of holes. This arises from the limited solubility of the doped elements within the ZnO lattice and the charge compensation effect between doped acceptors and V_O. In addition, the incorporation of doped group III elements, including Ga, In, Sc, B, and Al, into the ZnO lattice facilitates n-type conduction. In contrast, a more varied range of metallic elements, specifically from groups I, II, and III, into SnO_2 for doping, rather than using ZnO, has the potential to produce a p-type semiconductor with greater hole concentration. Nevertheless, as previously mentioned, the issue of charge compensation between substituted acceptors and inherent V_O defects persists within the host lattice when SnO_2 doping single metal such as Ga, Zn and In.[33–35] In order to eliminate or reduce the effects of charge compensation, an investigation of N incorporation into the SnO_2 lattice at V_O sites was conducted. Recent research has suggested that simultaneous doping with dual dopants such as Al–N, Ga–N, Zn–N, and Sb–N,[36–43] can help decrease charge compensation or release holes from substituted acceptors in SnO_2. In fact, studies have revealed that single metal doping (Ga, Zn, or In) in SnO_2 results in a low hole concentration of around 10^{18} cm^{-3},[33–35] but dual metal-N doping in SnO_2 achieves a concentration of 10^{20} cm^{-3}, signifying an enhancement

[a]*Faculty of Physics & Engineering Physics, VNUHCM-University of Science, Ho Chi Minh City 70000, Vietnam. E-mail: ltran@hcmus.edu.vn*

[b]*Vietnam National University Ho Chi Minh City, Ho Chi Minh City 70000, Vietnam*

of two orders of magnitude.[36,38,41–43] A dual In–N dopant could be a viable alternative to dual mentioned dopants, as long as the charge compensation effect is kept to a minimum. Nonetheless, the current research does not address the role of lowering charge compensation in In–N dual doped SnO_2 films. To address these challenges, this work describes generating In–N dual doped SnO_2 films with varying N concentrations in a mixed sputtering environment using direct current magnetron sputtering.

2. Materials and methods

2.1. Deposition of In–N dual doped SnO_2 films

In this study, In–N dual doped SnO_2 (INTO-x) films were grown on quartz and Si substrates employing a direct current sputtering technique in a mix of Ar and x% N_2 ($x = 0$, 15, 30, 45, and 60) gas at a working pressure of 10^{-3} torr. Substrates were heated at 300 °C before depositing films. The production of the In_2O_3-doped SnO_2 (INTO) ceramic target consisted of combining 95 wt% SnO_2 Merck powder with a purity of 99.999% and 5 wt% In_2O_3 Merck powder with a purity of 99.999%. This mixture was then subjected to grinding, drying, and hydraulic pressing to form a circular disc with a radius of 1.5 inches. Finally, the disc underwent six hours of sintered operation at 1500 °C. The German-made Leybold Univex 450 vacuum chamber was evacuated to 10^{-6} torr of pressure prior to the thin-film fabrication process. A high-purity mixed gas, with each gas type having a purity level of 99.9999%, was delivered into the vacuum system *via* two flowmeters adjusted to the appropriate rate. The INTO-x films were produced with a power of 80 W and a substrate-target distance of 8 cm. The cleaning process for the quartz substrates included the utilization of deionized water, acetone, and sodium hydroxide. On the other hand, the Si substrates were cleaned using trichloroethylene, isopropanol, diluted hydrofluoric acid, deionized water, and acetone. The substrates were desiccated using a stream of pure N_2 gas. The experiment utilized n-type Si (100) substrates possessing the resistivity ranging from 1 to 10 Ω cm and the carrier concentration of 1×10^{16} cm^{-3}.

2.2. Techniques for characterization

The transparency of the INTO-x/quartz films was assessed by analyzing the transmittance spectra in the wavelength range of 190–1100 nm using a V-630 system manufactured by JASCO in Japan. Electrical characteristics were determined at a temperature of 30 °C by measuring Hall equipped with an HL5500PC system manufactured by Nanometrics Incorporated, USA. The elemental compositions of the films were analyzed utilizing microscopy, which is enhanced by electron scanning accompanied by field emission (EDX) with the JSM-IT800 instrument manufactured by JEOL in Japan. The films' atomic compositions were examined using X-ray photoelectron spectroscopy (XPS) spectra, specifically the AXIS Ultra DLD instrument by KRATOS-SHIMADZU in Japan. X-ray diffraction (XRD) studies were conducted to verify the structural parameters of the INTO films, such as the dimensions of the crystal grains, the nature of the lattice planes, and any alterations in the diffraction angles. The analysis utilized a Shimadzu 6100 diffractometer, made by SHIMADZU CORPORATION in Japan, which was outfitted with a copper-K_α radiation source and the 2θ scan step of 0.01° is set up. Morphological examinations were performed utilizing microscopy, which is enhanced by electron scanning accompanied by field emission (FESEM, JSM-IT800). The smoothness of the surface was evaluated using microscopy based on atomic force interaction (AFM) with a Bruker Dimension Edge system. The conversion of photon energy to electrical energy was assessed by analyzing the current–voltage graphs derived from experiments conducted under both light and non-illuminated conditions. The measurements were performed using a Keithley source, namely the model 2450, in conjunction with a simulated AM 1.5 solar source.

3. Analysis results and discussion

3.1. Elemental composition of INTO-x films *via* EDX analysis

To accurately ascertain the oxygen concentration in INTO films *via* EDX analysis, the films were deposited on Si wafer. The EDX spectra of the INTO-x films in Fig. 1 shows binding energy peaks locating at 0.39 and 0.52 keV, attributed to N and O Kα_1 characteristic peaks, respectively, whereas a peak at around 3.29 keV corresponds to the Lα_1 distinctive binding energy of Indium. Additionally, the binding energy peaks were seen at 3.44, 3.66, and 3.9 keV, corresponding to the distinctive peaks of Sn including Lα_1, Lβ_1, and Lβ_2. Fig. 2 presents a colour map of all elements, illustrating a uniform elemental distribution over the entire sample. The atomic composition results of the INTO-x films, deposited according to the experimental settings outlined in Section 2, are presented in Table 1, demonstrating fluctuations in N and O atomic concentrations relative to x whereas the Sn and In concentrations remained nearly constant. This indicates that the presence of N-substituted O in the SnO_2 lattice. Furthermore, the r ratio, defined as the ratio of total of (O + N) to that of (Sn + In) content, was low for $x = 0$ and 15, but it

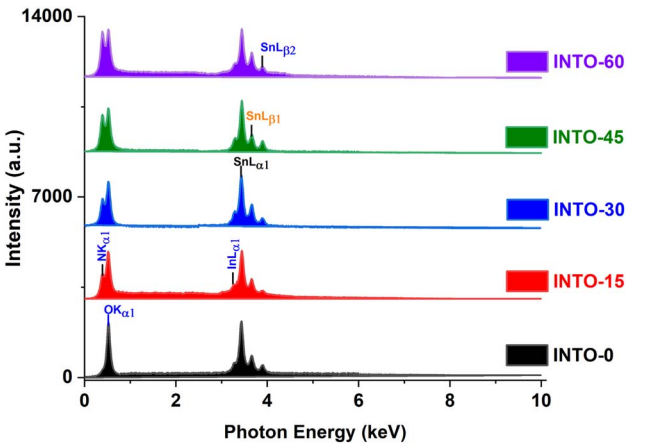

Fig. 1 EDX spectra of INTO-x films deposited on silicon substrates at 300 °C and 10^{-3} torr, with different percentages of N_2 in a mixed sputtering gas.

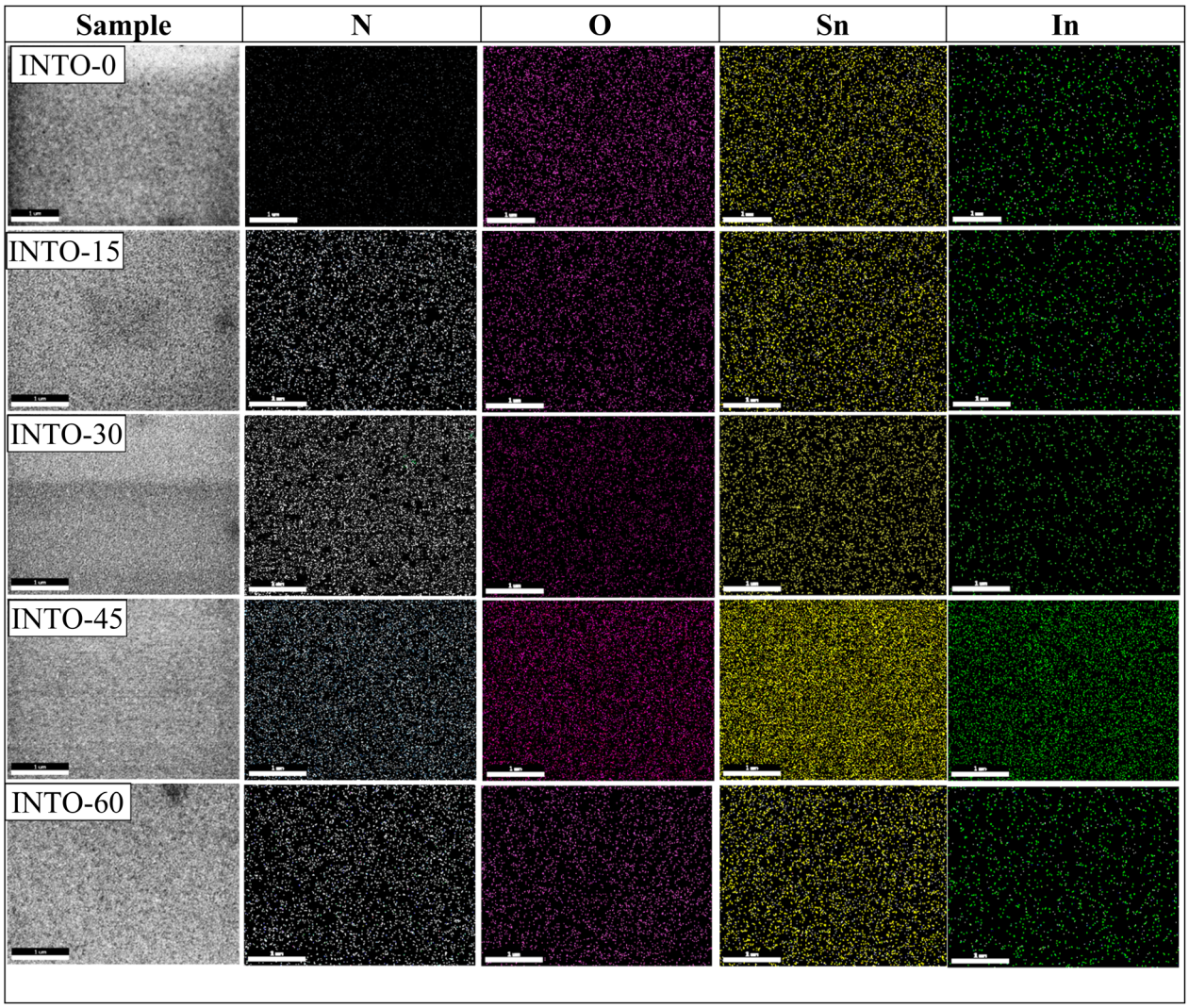

Fig. 2 EDX mapping images of INTO-*x* films deposited on quartz substrates at 300 °C and 10^{-3} torr, with different percentages of N_2 in a mixed sputtering gas.

approached 2 (1.91–1.94) when *x* exceeded than 15, thus aligning closely with the stoichiometry of SnO_2. This signifies that O was substituted by N. The *r* ratio increased with *x*, indicating oxygen vacancies (V_O) within the SnO_2 lattice decreases as *x* rises. To further exactly determine the atomic content of INTO-*x*, X-ray photoelectron spectroscopy is employed to complement the EDX study.

Table 1 Atomic composition of INTO-*x* samples with differing percentages of N_2 in a mixed sputtering gas, as determined from EDX analysis

Sample	% at. N	% at. O	% at. Sn	% at. In	$r \approx \frac{\%\ \text{at.}\ (O+N)}{\%\ \text{at.}\ (Sn+In)}$
INTO-0	1.04	61.81	32.5	4.65	1.69
INTO-15	10.46	54.61	30.31	4.62	1.86
INTO-30	14.62	51.06	29.64	4.68	1.91
INTO-45	17.68	48.23	29.41	4.68	1.93
INTO-60	18.74	47.28	29.36	4.62	1.94

3.2. Atomic composition of INTO-*x* films *via* XPS analysis

Fig. 3 displays the XPS core-level energy peaks of all elements of the INTO-*x* films, where *x* ranging from 0 to 60 in increments of 15. All XPS core-level energy peaks are calibrated based on C 1s binding energy peak at 284.5 eV. Fig. 3A indicates that the N 1s core-level energy is located at 396.9 eV, which is ascribed to the *N*-substituted O positions within the SnO_2 crystal lattice. Fig. 3B presents the In $3d_{5/2}$ to $3d_{3/2}$ double core level energy peak, ranging from 444.7 to 452.3 eV, attributed to the substitution of Sn^{4+} by In^{3+}. Also, Fig. 3C exhibits a Sn $3d_{5/2}$ to $3d_{3/2}$ double core-level peak located between 486.6 and 495 eV, attributed to the Sn–O bonding. Whereas Fig. 3D shows the O 1s binding energy peak at 530.5 eV, which was split into three sub-peaks: one at 530 eV, corresponding to the sufficient Sn–O bond, one at 531 eV, relating to the Sn–O bond influenced by V_O, and another at 532.5 eV, associated with the surface absorbed O kinds. The atomic composition of INTO-*x* is given in Table 2, where the atomic percentage was determined using the

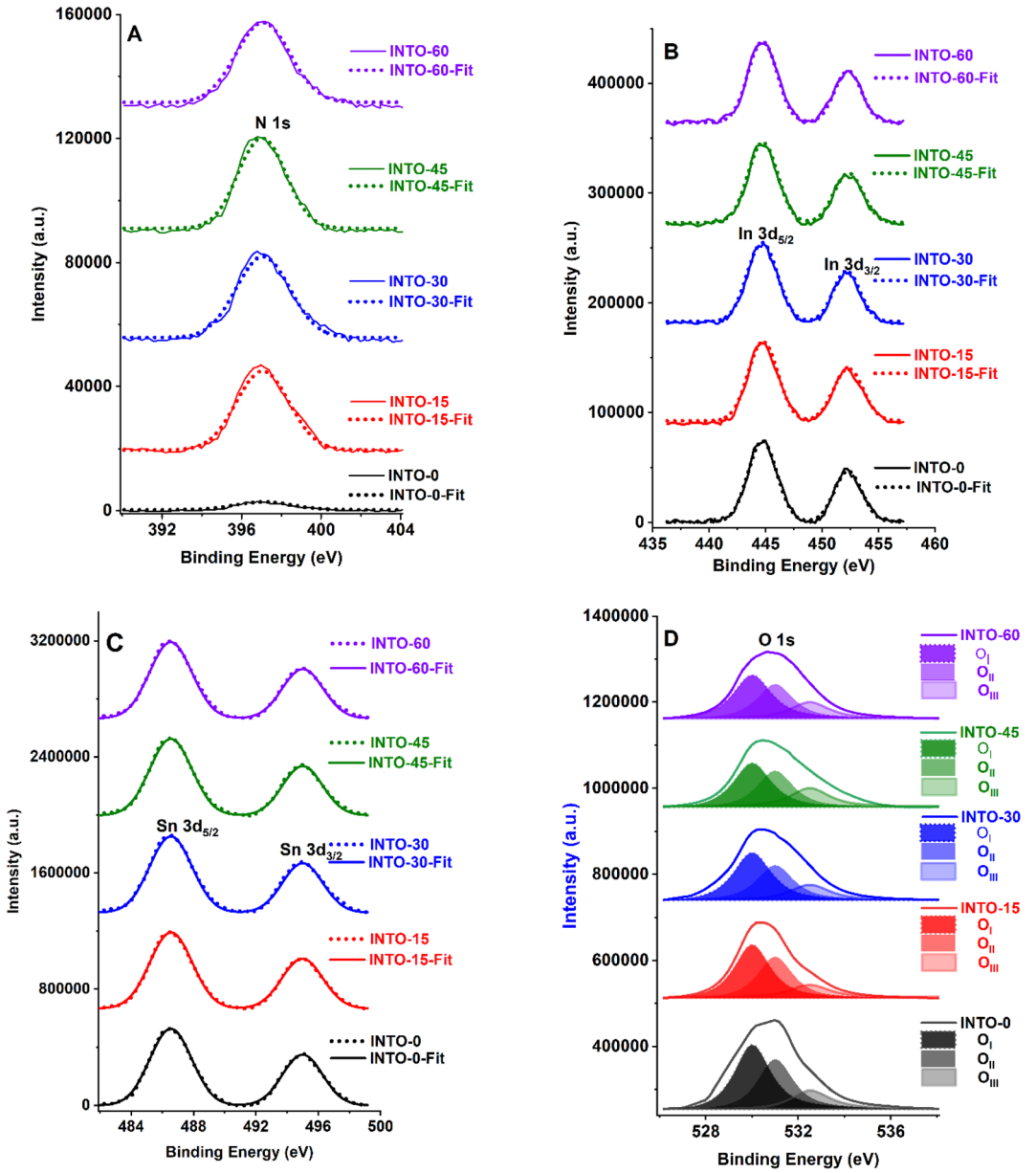

Fig. 3 XPS spectra of INTO-*x* films deposited on quartz substrates at 300 °C and 10^{-3} torr, with different percentages of N_2 in a mixed sputtering gas.

formula, $N_i = \frac{\frac{I_i}{S_i}}{\sum \frac{I_j}{S_j}}$ with i and j denoting In, N, O, or Sn. S and I denote atomic sensitivity parameters and the area of the core-level distinctive energy peaks.[44] The results indicate that the r ratio escalates when x increases, particularly reaching 1.93–1.96 when x is between 30 and 60. The results vary slightly from those obtained through EDX analysis, as XPS can detect oxygen in regions with oxygen vacancies, whereas EDX fails to identify such locations of oxygen vacancies. These data further demonstrate that the lattice points of *N*-substituted O increases

Table 2 Atomic composition of INTO-*x* samples with differing percentages of N_2 in a mixed sputtering gas, as determined from XPS analysis

Sample	% at. N	% at. O_1	% at. O_2	% at. O (% at. O_1 + % at. O_2)	% at. Sn	% at. In	$r \approx \frac{\%\ \text{at.}\ (O+N)}{\%\ \text{at.}\ (Sn+In)}$
INTO-0	1.21	35.66	26.45	62.11	32.16	4.52	1.73
INTO-15	10.52	31.55	23.31	54.86	30.07	4.55	1.89
INTO-30	14.71	29.36	21.81	51.17	29.59	4.53	1.93
INTO-45	17.77	27.87	20.42	48.29	29.48	4.46	1.95
INTO-60	18.97	27.16	20.11	47.27	29.25	4.51	1.96

Table 3 A structural data of INTO-x deposited on quartz substrates at 300 °C and 10^{-3} torr, with different percentages of N_2 in a mixed sputtering gas calculated XRD patterns

Sample	Phase-(hkl) peak of SnO_2	2θ (degree)	Full-width at half-maximum (FWHM) (rad)	Crystalline size D (nm)	Average crystalline size D (nm)	Lattice constant (Å)
INTO-0	Rutile (101)	33.86	0.57	14.57		a_{200} (= b) 4.6312
	(200)	38.88	0.51	16.53	13.40	
	(211)	51.53	0.81	10.89		c = 2.6377
INTO-15	Rutile (101)	33.81	0.59	14.08	17.88	a_{111} 5.0652
	Cubic (111)	30.56	0.38	21.68		
INTO-30	Rutile (101)	33.75	0.62	13.40	18.14	a_{111} 5.0700
	Cubic (111)	30.53	0.36	22.89		
INTO-45	Cubic (111)	30.50	0.32	25.74	25.74	a_{111} 5.0749
INTO-60	Cubic (111)	30.32	0.51	16.15	16.15	a_{111} 5.1043

with x, indicating the XPS results are consistent with those of the EDX investigation, as detailed in Section 3.1. Thus, EDX and XPS investigations indicate that the presence of N-substituted O lattice points inside the host lattice escalated with x value, confirming the quantity of N-substituted O elements within the host lattice rises, as seen in Tables 1 and 2.

3.3. Structural characteristics of INTO-x films *via* XRD patterns

The crystal structure of undoped SnO_2 films is typically tetragonal rutile, irrespective of the deposition process, and this rutile phase remains unchanged when SnO_2 films are doped with metal elements such as Sb, In, Ga, and Zn, particularly when employing the dc magnetron technique.[33–35] However, Al–N, Ga–N, Zn–N, and Sb–N -doped SnO_2 films produced *via dc* magnetron technique showed a phase transition from rutile to cubic which is ascribed to the incorporation of N into SnO_2 lattice.[36,38,41–43] The crystal structure of In–N doped SnO_2 showed the same phase transition as Al–N, Ga–N, Zn–N, and Sb–N -doped SnO_2 films, as illustrated in Table 3 and Fig. 4. Fig. 4 shows In-doped SnO_2 (INTO-0) possesses rutile phase characterized by three lattice reflections (101), (200) and (211), located at 2θ = 33.86, 38.88, and 51.53°, respectively. When In-doped SnO_2 is deposited using a mixed sputtering gas containing 15% N_2, a decline in the rutile reflection (101) is observed, alongside a total lack of rutile reflection (200), and the emergence of cubic reflection (111) at 2θ = 30.56°. This indicates the incorporation of N into the SnO_2 lattice. A more distinct phase transition indicates greater degradation of the rutile reflection (101) and increased evolution of the cubic reflection (111). Consequently, the observation of solely the cubic reflection (111) along with a maximum crystal grain size of 25.74 nm suggests that the rutile-to-cubic phase transition is fully achieved at x = 45, which aligns with the deposition of INTO in a mixed sputtering gas comprising 45% N_2. Table 3 indicates that optimal crystal quality is achieved with the maximum crystal grain size, as calculated using Scherer equation;[27] nevertheless, crystal deterioration reoccurs when x exceeds 45, attributed to an excessive quantity of N-substituted O elements in the host lattice or the exceeding of the crystal structure's stability threshold. Table 3 additionally illustrates the N incorporation into the SnO_2 lattice, as indicated by the 2θ shift of all reflections to the lower values with increasing x. Besides, the crystal grain size of cubic reflection (111) increases with x until x reaches 45, after which it falls when x exceeds 45, proving the substitution of O by N. This suggests that films with higher number of V_O defects cause lattice distortion, thereby leading to poor crystal quality. Consequently, the incorporation of N into the SnO_2 lattice corresponds to a reduction in the number of V_O defects, leading to an increase in the crystal grain size of the cubic reflection (111) with increasing x. However, when x exceeds 45, crystal degradation occurs, resulting in a decrease in crystal grain size due to significant lattice broadening. Furthermore, lattice parameter of cubic reflection (111) increases with rising x, signifying that the quantity of N-substituted O elements rises with x.

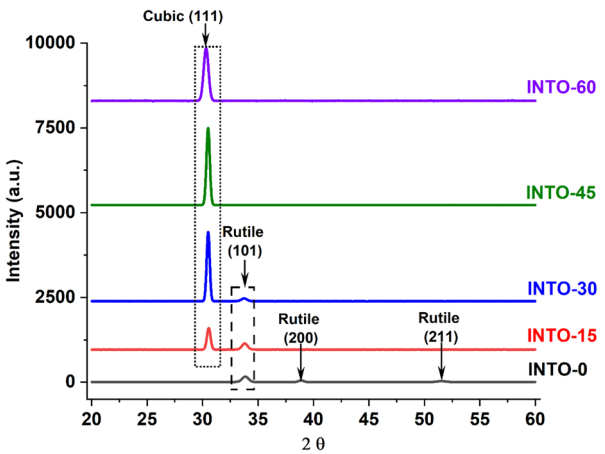

Fig. 4 XRD patterns of INTO-x films deposited on quartz substrates at 300 °C and 10^{-3} torr, with different percentages of N_2 in a mixed sputtering gas.

3.4. Morphology of INTO-x films *via* FESEM

FESEM research complements XRD patterns for further investigation of the crystal structure influenced by the substitution of O with N in the SnO_2 lattice. Fig. 5 displays FESEM images, encompassing surface and cross-sectional views, as well as the grain size distribution of INTO-x films. The results reveal that grain size grows with rising x until x equals 45; thereafter, it

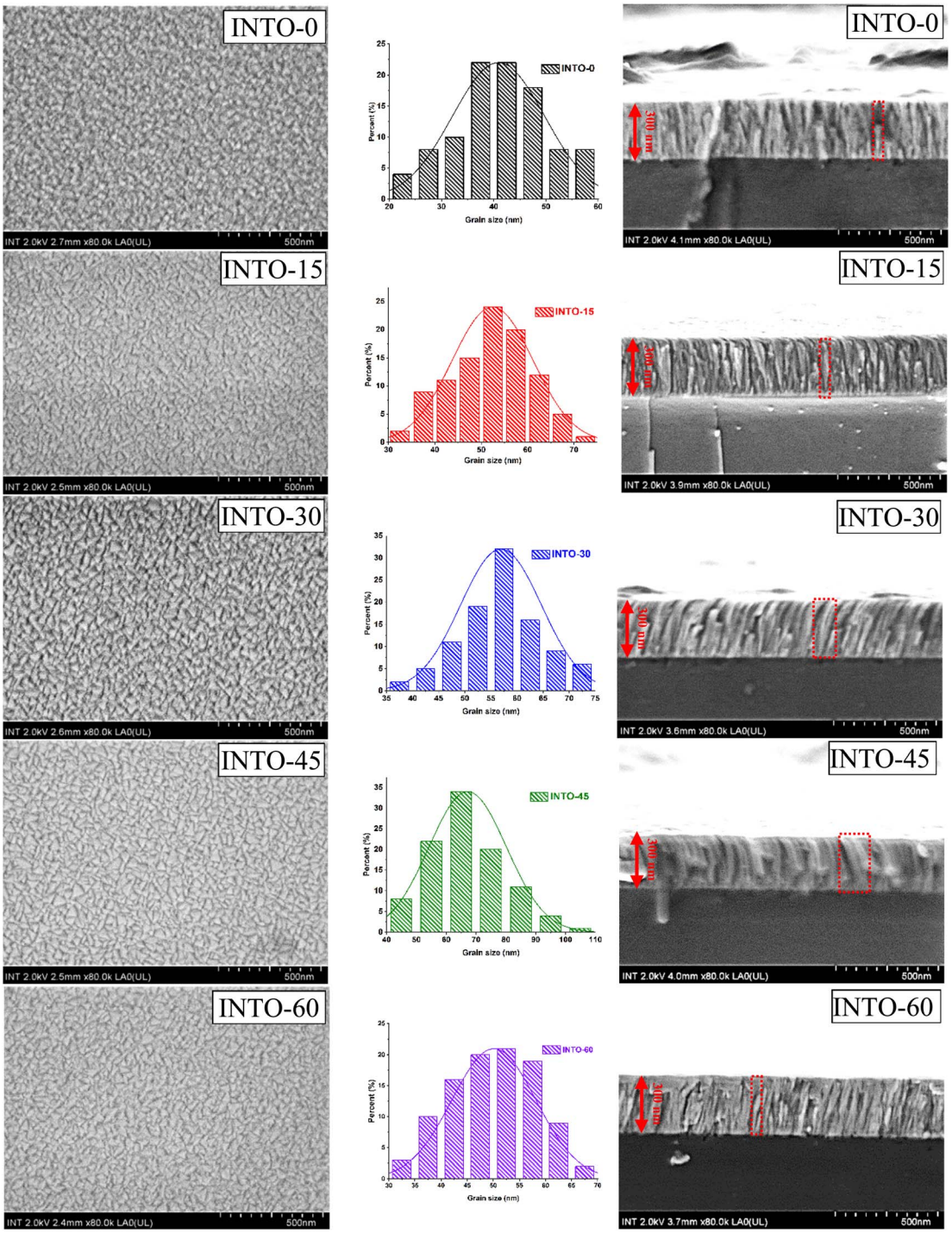

Fig. 5 FESEM images and grain size distribution spectra of INTO-x films deposited on quartz substrates at 300 °C and 10^{-3} torr, with different percentages of N_2 in a mixed sputtering gas.

drops at $x = 60$, suggesting the presence of N-substituted O sites in the SnO_2 lattice, which aligns with the study in Section 3.3. The top and side images from FESEM further illustrate that the replacement of O with N results in a denser structure, notably noticeable in the most compact structure of INTO-45. The maximum grain size of 68 nm for the INTO-45 film is demonstrated by the grain distribution, which further implies that the fluctuations in grain size match those seen in XRD analysis. Besides, cross-sectional images demonstrate that all of the films have a thickness of about 300 nm, exhibiting different widths throughout the samples as indicated in Fig. 5.

3.5. Morphology of INTO-x films *via* AFM

AFM images depict the surface morphology of films at the microscale, in of the surface smoothness of films diminishes

Table 4 Average crystalline size, root mean square and bandgap of INTO-x samples with different percentages of N_2 in a mixed sputtering gas

Sample	% at. N	Average crystalline size D (nm)	RMS (nm)	Bandgap (eV)
INTO-0	1.21	13.40	1.63	4.18
INTO-15	10.52	17.88	1.21	3.96
INTO-30	14.71	18.11	1.18	3.79
INTO-45	17.77	25.74	0.61	3.73
INTO-60	18.97	16.15	1.31	3.45

progressively with increasing x until x reaches 45, which corresponds to the minimum surface smoothness or root mean square (RMS), attributed to the most quantity of N-substituted O spots within the host lattice. This demonstrated that the crystal quality improves, aligning with FESEM and XRD investigations. The dense surface of the FESEM image signifies a reduction in grain boundaries, leading to a decrease in the RMS of the AFM images. However, when films are deposited at x value over the threshold value of 45, the surface compactness observed in FESEM decreases which is the sequence of reducing N-substituted O points in the SnO_2 lattice, which subsequently leads to an increase in RMS values in AFM images thereafter. In addition, Table 4 illustrates the correlation among average crystalline size, root mean square, and band gap of INTO-x samples in relation to varying amounts of different N_2 in a mixed sputtering gas. The findings suggest that the number of V_O defects diminishes with an escalation in N–V_O substitution within the SnO_2 lattice, resulting in an enhancement in film density. Notably, the highest film density or the largest average crystal size was associated with an optimal quantity of N-substituted O sites in the SnO_2 lattice when $x = 45$, which is consistent with the literature.[41,42] Furthermore, the band gap of INTO-x decreases with x, which is due to an increase in N-substituted O sites in the SnO_2 lattice as explained in the next section (Fig. 6).

3.6. Optical transmittance spectra of INTO-x films

The optical transmittance spectra of INTO-x films were measured within the region of 200–1100 nm, as illustrated in Fig. 7A. The results indicate that the red shift of absorption edge occurs when x increases, attributed to the incorporation of N

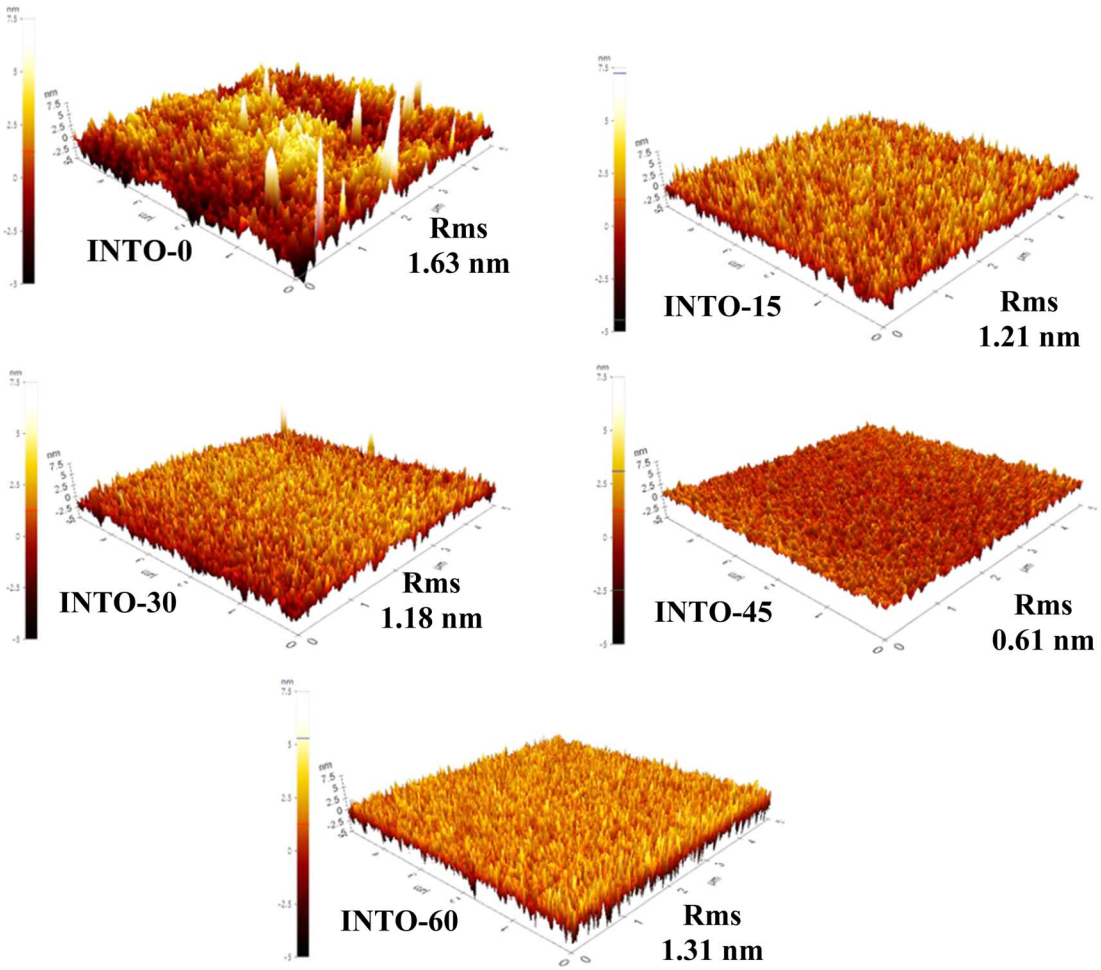

Fig. 6 AFM images of INTO-x films deposited on quartz substrates at 300 °C and 10^{-3} torr, with different percentages of N_2 in a mixed sputtering gas.

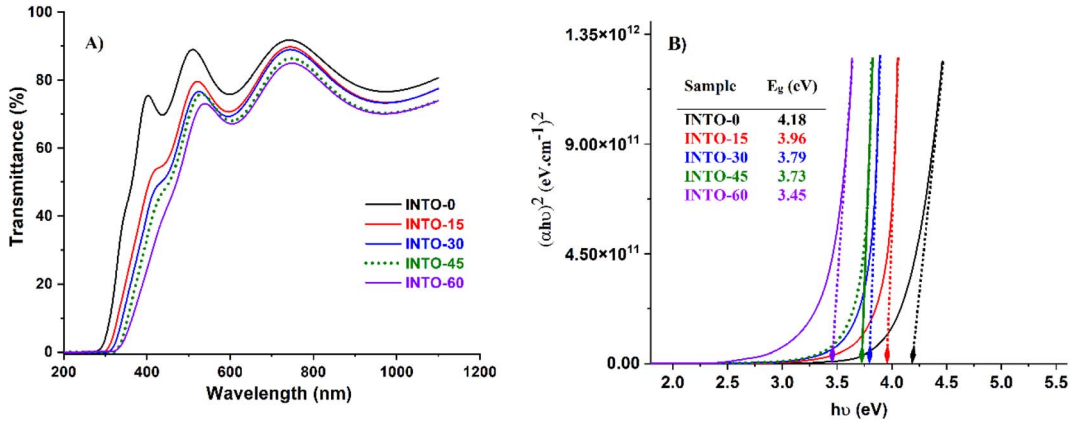

Fig. 7 Transmittance spectra (A) and bandgap energy (B) of INTO-*x* films deposited on quartz substrates at 300 °C and 10^{-3} torr, with different percentages of N_2 in a mixed sputtering gas.

into the SnO_2 lattice as discussed in the literature.[36,38,41–43] The red shift of absorption edge indicates a reduction in bandgap energy, as illustrated in Fig. 7B. This is determined based on Tauc equation, where the $(\alpha h\nu)^2$ is a function of $h\nu$ and the absorption coefficient (α) is a function varies with wavelength, as inferred from simulations performed with the Scout software. The findings show that the bandgap energy diminishes with the augmentation of *N*-substituted O elements in the SnO_2 lattice, as ascertained through the EDX and XPS investigations in Sections 3.1 and 3.2.

3.7. Electrical characteristics of INTO-*x* films

Despite containing approximately 4.5 at% In^{3+}, INTO-0 functions as an n-type semiconductor, signifying that the V_O donors prevail over the acceptors In^{3+}. Therefore, N is doped into SnO_2 to create p-type conductive SnO_2 due to the integration of N^{3-} acceptors into the host lattice. Table 5 demonstrates that the hole concentration of INTO films escalates with increasing *x*, signifying that N incorporation into the SnO_2 lattice functions as acceptors, which aligns with the absorption edge of the transmittance spectra reported in Section 3.6. The results demonstrate that hole mobility increases with *x*, attributed to a decrease in V_O in SnO_2 and an improvement in crystal quality. The substitution of V_O sites with N in the SnO_2 lattice diminishes the attractive interaction between charge carriers and V_O defects, as well as minimizes charge carrier scattering caused by V_O defects. Furthermore, improved crystal quality diminishes charge carrier scattering at grain boundaries, aligning with literature reports.[41,42] The INTO-45 film shows the lowest resistivity of 5.1×10^{-3} Ω cm and the highest hole mobility of 12.75 $cm^2\ V^{-1}\ s^{-1}$. In contrast, the resistivity of the INTO-60 film rises while hole mobility decreases, which is indicative of crystal degradation, aligning with the XRD results presented in Section 3.3.

3.8. Testing photo-electrical effect of INTO-*x*/Si

All of INTO-*x* (where *x* ranges from 15 to 60) is deposited on Si substrates to examine the photo-electronic effects of the p–n junction, with the *I*–*V* measurement conditions detailed in Section 2.2. The current (*I*) – voltage (*V*) characteristics of In/INTO-*x* and In/Si interfaces exhibit linear behavior, indicating ohmic contact, and are not illustrated here. Fig. 8A illustrates a schematic structural model for assessing the photoelectronic effect at the INTO/Si interface. Fig. 8B illustrates the dark *I*–*V* characteristics of In/INTO-*x*/Si/In, exhibiting non-linear or rectified behavior, hence indicating that INTO-*x* functions as a p-type semiconductor. The findings indicate that the dark reverse bias current of In/INTO-45/Si/In is optimized owing to enhanced crystal quality, reduced RMS value, and minimal resistivity. Under illumination, the reverse bias current of all INTO-*x*/Si interfaces substantially increases compared to the dark reverse bias current, as the generated internal electric field accelerates photocarriers toward the two indium electrodes. The photocurrent at the INTO-45/Si interface under reverse bias is maximal, signifying that INTO-45 exhibits the most advantageous electrical and structural characteristics. The

Table 5 Resistivity, carrier concentration and carrier mobility of INTO-*x* films deposited on quartz substrates at 300 °C and 10^{-3} torr, with differing percentages of N_2 in a mixed sputtering gas

Samples	Resistivity ρ (Ω cm)	Mobility μ ($cm^2\ V^{-1}\ s^{-1}$)	Carrier concentration *n* (cm^{-3})	Type
INTO-0	4.5×10^{0}	1.24	-1.12×10^{18}	n
INTO-15	7.5×10^{-2}	2.58	3.23×10^{19}	p
INTO-30	1.5×10^{-2}	5.13	8.12×10^{19}	p
INTO-45	5.1×10^{-3}	12.75	9.61×10^{19}	p
INTO-60	9.0×10^{-3}	6.43	1.05×10^{20}	p

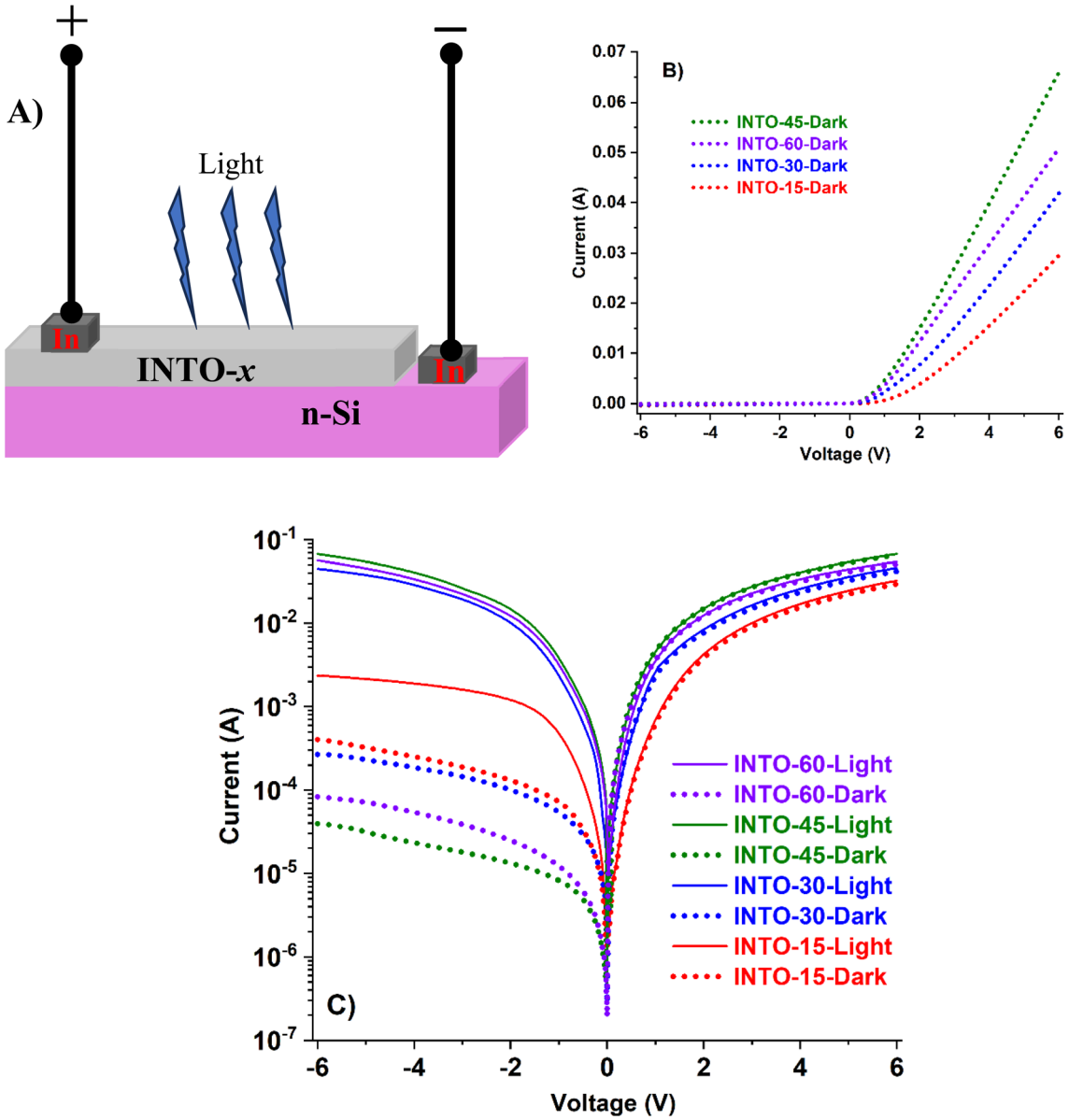

Fig. 8 *I–V* characteristics of INTO-*x* films deposited on Si substrates at 300 °C and 10^{-3} torr, with different percentages of N_2 in a mixed sputtering gas.

photocurrent value is proportional to with the crystal quality and electrical characteristics of the films.

4. Conclusion

Investigations using EDX and XPS verified that N^{3-} had replaced O^{2-}. The redshift of the absorption edge in transmittance spectra, an increase in hole concentration, an improvement in crystal quality, and an increase in reverse photocurrent of INTO/Si interfaces all indicate that the amount of *N*-substituted O elements in SnO_2 increases with the N_2 content in mixed sputtering gas. The ideal characteristics of the INTO-45 film, which is deposited in 45% N_2 of the mixed sputtering gas, include the maximum hole mobility of 12.75 $cm^2\ V^{-1}\ s^{-1}$ which is surpassed only by that of SnO_2 doped with Zn–N (15.6 $cm^2\ V^{-1}\ s^{-1}$), the lowest roughness of 0.61 nm – lower than that of SnO_2 doped with Zn–N, Sb–N, Al–N, and Ga–N, the lowest resistivity of 5.1×10^{-3} Ω cm which is exceeded solely by SnO_2 doped with Zn–N (3.8×10^{-3} Ω cm), and the highest crystal grain size of 25.74 nm. The outcomes provide maximal photocurrent for INTO-45/Si interface.

Data availability

All data relevant for the reproduction of the results presented in this work are included within the article.

Conflicts of interest

There are no conflicts to declare.

Acknowledgements

This research is funded by University of Science, VNU-HCM under grant number T2024-09.

References

1 V. Sittinger, H. King, A. Kaiser, S. Jung, Ö. Ş. Kabakli, P. S. C. Schulze and J. C. Goldschmidt, *Surf. Coat. Technol.*, 2023, **457**, 129286.
2 T. Hölscher, M. Placidi, I. Becerril-Romero, R. Fonoll-Rubio, V. Izquierdo-Roca, A. Thomere, E. Bailo, T. Schneider, H. Kempa, R. Scheer and A. Pérez-Rodríguez, *Sol. Energy Mater. Sol. Cells*, 2023, **251**, 112169.
3 N. Ohashi, R. Kaneko, C. Sakai, Y. Wasai, S. Higuchi, K. Yazawa, H. Tahara, T. Handa, T. Nakamura, R. Murdey, Y. Kanemitsu and A. Wakamiya, *Sol. RRL*, 2023, **7**, 2300221.
4 I. - Haq, M. I. Khan, M. Irfan, M. Fatima, H. H. Somaily, Z. M. Elqahtani and N. Alwadai, *Ceram. Interfaces*, 2023, **49**, 29622–29629.
5 S. K. Swami, J. I. Khan, V. Dutta, J. Lee, F. Laquai and N. Chaturvedi, *ACS Appl. Energy Mater.*, 2023, **6**, 2906–2913.
6 H. W. Lee, S. Biswas, H. Choi, Y. Lee and H. Kim, *Appl. Surf. Sci.*, 2024, **659**, 159930.
7 Z. Yan, J. Shi, S. Chen, J. Du, L. Zhang, Q. Yuan, C. Song, K. Jiang, Y. Yang, A. Han, Z. Liu and F. Meng, *Sol. Energy Mater. Sol. Cells*, 2023, **253**, 112244.
8 F. Ceh-Cih, E. Camacho-Espinosa, I. Rimmaudo, R. Mis-Fernández, S. Uc-Canché and J. L. Peña, *Sol. Energy*, 2024, **273**, 112549.
9 R. Ramarajan, N. Purushothamreddy, R. K. Dileep, M. Kovendhan, G. Veerappan, K. Thangaraju and D. Paul Joseph, *Sol. Energy*, 2020, **211**, 547–559.
10 J. Zhou, X. Zhang, H. Chen, Z. Tang, D. Meng, K. Chi, Y. Cai, G. Song, Y. Cao and Z. Hu, *Appl. Surf. Sci.*, 2020, **534**, 147632.
11 N. Gagrani, K. Vora, S. Adhikari, Y. Jiang, C. Jagadish and H. H. Tan, *Adv. Opt. Mater.*, 2022, **10**, 2102690.
12 S. González, G. Vescio, J. L. Frieiro, A. Hauser, F. Linardi, J. López-Vidrier, M. Oszajca, S. Hernández, A. Cirera and B. Garrido, *Adv. Mater. Interfaces*, 2023, **10**, 2300035.
13 J. Jing, L. Lin, K. Yang, H. Hu, T. Guo and F. Li, *Org. Electron.*, 2022, **103**, 106466.
14 M. N. Rezaie, S. Mohammadnejad and S. Ahadzadeh, *Opt. Laser Technol.*, 2021, **138**, 106896.
15 Y. J. Kim, B. W. Kim and S. H. Im, *Adv. Mater. Interfaces*, 2024, **11**, 2400020.
16 S. Sreekumar, V. Bruevich, V. Podzorov and D. M. O'Carroll, *Appl. Surf. Sci.*, 2024, **670**, 160596.
17 B. S. Sannakashappanavar, A. B. Yadav, K. Singh and T. A. Sai, *Micro and Nanostructures*, 2023, **179**, 207581.
18 R. A. Rodriguez-Davila, R. A. Chapman, Z. H. Shamsi, S. J. Castillo, C. D. Young and M. A. Quevedo-Lopez, *Microelectron. Eng.*, 2023, **279**, 112063.
19 C. Avis, M. M. Billah and J. Jang, *Adv. Photonics Res.*, 2024, **5**, 2300215.
20 W. Jin, K. Park, J. Y. Cho, S.-H. Bae, M. Siyar, H. Jang and C. Park, *Ceram. Interfaces*, 2023, **49**, 10437–10444.
21 Z. Fang, S. Tian, B. Li, Q. Liu, B. Liu, X. Zhao and G. Sankar, *Appl. Surf. Sci.*, 2021, **540**, 148414.
22 H. Liu, H. Zong, L. Yan, D. Zhou, Y. Yin, G. Cao, L. Bian, C. Kang and M. Li, *Infrared Phys. Technol.*, 2021, **113**, 103648.
23 S. J. Lee, S. H. Lee, H. W. Kang, S. Nahm, B. H. Kim, H. Kim and S. H. Han, *Chem. Eng. J.*, 2021, **416**, 129028.
24 A. Olkun, S. Pat, N. Akkurt, R. Mohammadigharehbagh, U. Demirkol, M. Özgür and Ş. Korkmaz, *J. Mater. Sci.: Mater. Electron.*, 2020, **31**, 19074–19084.
25 Y. Hu, L. Xiong, X. Cai, Z. Lin, X. Zhou, J. Zhang, X. Tang, Y. Zhan and J. Luo, *Sol. Energy Mater. Sol. Cells*, 2024, **274**, 112960.
26 A. L. C. Silva, L. M. Bolaños Vargas, M. L. Peres, A. D. G. Rodrigues, A. J. Chiquito, M. D. Teodoro and M. P. F. De Godoy, *J. Alloys Compd.*, 2024, **1004**, 175761.
27 N. H. Erdogan, T. Kutlu, N. Sedefoglu and H. Kavak, *J. Alloys Compd.*, 2021, **881**, 160554.
28 W. Li, H. Zhang, X. Zhang, G. Qin, H. Li, Y. Xiong, L. Ye, H. Ruan, C. Tong, C. Kong and L. Fang, *Appl. Surf. Sci.*, 2020, **529**, 147168.
29 L. Cao, L. Zhu and Z. Ye, *J. Phys. Chem. Solids*, 2013, **74**, 668–672.
30 X. Nie, B. Zhang, J. Wang, L. Shi, Z. Di and Q. Guo, *Mater. Lett.*, 2015, **161**, 355–359.
31 S. Mondal and D. Basak, *Ceram. Interfaces*, 2022, **48**, 20000–20009.
32 T.-H. Feng and X.-C. Xia, *Opt. Mater. Express*, 2016, **6**, 3733.
33 H. P. Dang, Q. H. Luc, V. H. Le and T. Le, *J. Alloys Compd.*, 2016, **687**, 1012–1020.
34 T. Le, H. P. Dang, Q. H. Luc and V. H. Le, *J. Phys. D: Appl. Phys.*, 2017, **50**, 145102.
35 T. Le, H. P. Dang and V. H. Le, *J. Alloys Compd.*, 2017, **696**, 1314–1322.
36 T. T. A. Tuan, A. Q. Duong, N. Van Sau, H. P. Dang and T. Le, *Opt. Mater.*, 2021, **111**, 110665.
37 P.-M. Lee, Y.-S. Liu, L. Villamagua, A. Stashans, M. Carini and C.-Y. Liu, *J. Phys. Chem. C*, 2016, **120**, 4211–4218.
38 H. P. Dang, Q. H. Luc, T. T. Nguyen and T. Le, *J. Alloys Compd.*, 2019, **776**, 276–286.
39 S. Lv, Y. Zhou, W. Xu, W. Mao, L. Wang, Y. Liu and C. He, *Appl. Surf. Sci.*, 2018, **427**, 64–68.
40 Y. Zhou, W. Xu, S. Lv, C. Yin, J. Li, B. Zhu, Y. Liu and C. He, *J. Alloys Compd.*, 2018, **732**, 555–560.
41 H. Kim Dan, M. K. Pham, H. P. Dang, U. L. Quach, A. T. Dao and T. Le, *Mater. Sci. Semicond. Process.*, 2023, **155**, 107230.
42 N. T. K. Chung, H. P. Dang, T. P. Nguyen and T. Le, *J. Photochem. Photobiol., A*, 2021, **418**, 113436.
43 T. Le and H. P. Dang, *Sens. Actuators, A*, 2020, **316**, 112421.
44 B. V. Crist, *Handbooks of Monochromatic XPS Spectra – the Elements and Native Oxides*, XPS Inter-national LLC, Mountain View (CA, USA), 1999, vol. 1.